Modeling of Macrosegregation Due to Thermosolutal Convection and Contraction-Driven Flow in Direct Chill Continuous Casting of an Al-Cu Round Ingot

A.V. REDDY and C. BECKERMANN

Macrosegregation in direct chill (DC) continuous casting of an Al-4.5 wt pct Cu round ingot is numerically simulated. The model incorporates descriptions of heat transfer, solute redistribution, and melt convection on the system scale with microscopic relations for grain growth, solutal undercooling, and microsegregation. Simulations are conducted to study the effects of mushy zone permeability, thermosolutal convection, and solidification contraction on the macrosegregation pattern in a DC casting. The results indicate that centerline segregation can be either positive or negative, depending upon the grain density in and permeability of the mush. In addition, it is shown that the flow induced by solidification contraction not only causes inverse segregation at the ingot surface, but also has a significant influence on the macrosegregation across the central portion of the ingot. A comparison with temperature and macrosegregation patterns measured in a previous experiment shows reasonable agreement. Several areas for future model improvements are identified.

I. INTRODUCTION

MACROSEGREGATION continues to be one of the concerns in direct chill (DC) continuous casting of aluminum ingots. The variation in composition over the ingot cross section results in the need to adjust alloy composition in order to meet mechanical property specifications in finished products. The extent of macrosegregation is greatly affected by the casting conditions, such as casting speed, superheat, cooling rate, mold size, alloy composition, and grain-refining practices. Thus, it is of interest to develop a mathematical model to simulate macrosegregation in DC casting, enabling the selection of conditions that minimize macrosegregation while maintaining a high productivity.

Various mechanisms for macrosegregation in aluminum DC casting have been discussed by Chu and Jacoby[1] and Yu and Granger.[2] In general, macrosegregation is caused by the relative movement of liquid and solid in the mushy zone, because the alloy constituents have different solubilities in the two phases. One cause of interdendritic liquid flow through the rigid solid structure in the mushy zone is the contraction of the liquid and the density difference between the solid and liquid phases during solidification. The commonly observed inverse segregation pattern near the outer ingot surface is known to be the result of such contraction driven backflow of solute-rich liquid. Positive segregation at the ingot surface can also be caused by exudation of interdendritic liquid through channels in the partially solidified shell into the contraction gap between the shell and the mold. This flow is driven by the metallostatic head.[3–6] Less clear are the transport phenomena leading to either positive or negative segregation in the center region of the ingot. Flemings and co-workers[7,8,9] examined the effects of various interdendritic melt flows in the mushy zone due to thermal and solutal buoyancy forces on centerline segregation. Such melt flow is strongly affected by the permeability and, hence, the microstructure of the mushy zone. Finn *et al.*[10] concluded from their experiments that, for a grain-refined ingot, the mushy zone is more permeable and allows for the advection of the solute-rich liquid toward the centerline producing positive segregation there. On the other hand, the less permeable mushy zone in the case without grain refiner prohibited such advection and produced negative centerline segregation. Contrary to the observations of Finn *et al.*, negative centerline segregation has also been experimentally observed in grain-refined ingots.[1,2,11] These experiments indicate that liquid flow in the mushy zone can have a significant effect on centerline segregation. It has also been argued that the transport of broken/detached dendrites from the mold region to the ingot center by convection currents in the liquid pool tends to increase negative segregation at the ingot center.[1,2]

Numerous numerical models have appeared in the literature for simulating the coupled heat and fluid flow during aluminum DC casting.[12–20] Many of these studies have shown good agreements between measured and predicted temperature distributions. They have helped to understand the effects of (sometimes turbulent) natural and forced convection on the sump shape, the flows in the feeding and distributor system, the transients during startup, and the effects of various casting parameters on microstructure and ingot quality. Of particular interest to the present study are the ways in which the flows in the mushy zone have been modeled. Usually, the solid is assumed to be rigid and attached and the drag experienced by the interdendritic liquid is modeled using a permeability that gradually decreases with increasing solid fraction.[12,13,20] Other studies simply increase the viscosity[14,15] or force the liquid velocity in the mush to the casting speed above a certain solid fraction.[12] Although a stationary solid (relative to the casting speed)

A.V. REDDY, Postdoctoral Associate, Department of Mechanical Engineering, The University of Iowa, is with the Los Alamos National Laboratory, Los Alamos, NM. C. BECKERMANN, Professor, is with the Department of Mechanical Engineering, The University of Iowa, Iowa City, IA 52242-1527.

Manuscript submitted May 21, 1996.

was ultimately assumed, Flood *et al.*[13] introduced a so-called consolidation factor that varies linearly with solid fraction to take into account the movement of free, unattached solid. A two-phase model[21] was used in Reference 19 to calculate individual solid and liquid velocities during aluminum DC casting of a round ingot.

Comparably few researchers have attempted to model macrosegregation in DC continuous casting of aluminum alloys. The prediction of macrosegregation requires not only consideration of heat transfer and fluid flow, but also the solution of a solute transport equation. Fully coupled macrosegregation models have experienced considerable progress in the past 10 years, and comprehensive, recent reviews are available.[22,23] Flood *et al.*[13] pioneered the application of such a coupled model to DC casting of an Al-4.5 wt pct Cu ingot. The solid fraction was calculated using the lever rule and, consequently, the eutectic reaction was not modeled. While thermal and solutal buoyancy forces were taken into account, contraction-driven flow and exudation were not included in the model. The results indicated the presence of positive centerline segregation as a result of enriched, denser interdendritic liquid flowing toward the ingot center. The importance of solutal buoyancy forces was emphasized. No comparisons with experiments were reported. In a later study, Flood *et al.*[24] used scaling analysis to predict flow velocities and sump shapes in DC casting. These results are then used to make a number of qualitative predictions about the effects of certain casting parameters on macrosegregation. For example, centerline segregation is found to be more strongly influenced by ingot size than by casting speed, because a greater sump size promotes the fragmentation and growth of free crystals. Using the two-phase model, Reddy and Beckermann[19] were able to demonstrate the effect of solid movement on centerline segregation, but only preliminary results were presented.

Modeling of the macrosegregation near the outer surface in DC casting has received separate research attention by analyzing the region next to the chill surface only and limiting the model to unidirectional transport perpendicular to the surface. The model by Haug *et al.*[25] is the recent and most advanced example of such work and is relevant to DC casting, because it includes the combined effect of contraction driven flow and exudation. It was found that, in DC casting, both types of flow have a significant influence on macrosegregation close to the surface.

The objective of the present study is to develop a model to investigate the effect of thermosolutal buoyancy and contraction-driven mushy zone flows on macrosegregation in DC continuous casting of an Al-4.5 wt pct Cu round ingot. Important assumptions made in the model are that the transport of solid in the form of free grains and exudation are not taken into consideration. The first assumption can be justified in view of the fact that modeling of the fragmentation and transport of free solid is only at a preliminary stage, as evidenced by the calculations presented in Reference 19. Instead, it is shown in the following what macrosegregation patterns develop in the presence of a rigid and attached solid in the mush. The neglect of exudation will result in inaccuracies in the predicted macrosegregation pattern near the outer surface. The study uses a simplified version of the two-phase model of Ni and Beckermann[21] and employs a microscopic grain growth model that accounts for back-diffusion in the solid (microsegregation), solutal undercooling in the liquid, and the effect of different grain densities. The geometry and boundary conditions are patterned after the binary alloy experiments of Finn *et al.*,[10] because their experiments featured not only measurements of temperature but also of macrosegregation and grain structure. Comparisons with their experimental results are made and additional parametric studies are performed. Together, the results give an indication of the importance of accurately modeling the effect of grain structure on the flows in the mushy zone and, hence, macrosegregation.

II. MODEL DESCRIPTION

The model used in the present simulations is a simplified version of the two-phase model developed by Ni and Beckermann,[21,26] where the velocity of the solid phase is assumed to be equal to the casting speed everywhere. Tables I and II summarize the governing equations and supplementary relations, respectively. Only a few explanations are provided here, and the reader is referred to the original references for the details of the model and the assumptions made in the derivation.

The model assumes a globulitic microstructure. This can be considered a reasonable approximation for the relatively small spheroidal grains found in the grain-refined ingot in the experiments of Finn *et al.*[10] As is shown later, the model may also be approximately valid for non-grain-refined dendritic microstructures if the globular grains are viewed as secondary dendrite arms, although their shapes are somewhat different. An extension of the two-phase model to the equiaxed dendritic case has recently been presented by Wang and Beckermann.[30] In writing the energy equation, thermal equilibrium between the phases in an averaging volume has been assumed, *i.e.*, $T_s = T_l = T_i = T$, where T_i is the interfacial temperature. This is appropriate due to the high value of the Lewis number ($=\alpha/D$) for metal alloys. Note that species conservation equations are solved for both the liquid and solid phases. The interfacial species balance in Table I constitutes the microscopic grain growth model in the present set of equations. It states that the solute rejected upon solidification is either back-diffused in the solid or advected into the undercooled liquid. The two transport terms on the right-hand side of the interfacial species balance contain the interfacial area concentration and so-called diffusion lengths, expressions for which are provided in Table II. It has been shown elsewhere[31] that the present back-diffusion model gives accurate predictions of solid microsegregation and the final eutectic fraction. Keeping track of the eutectic fraction is important for the prediction of contraction-driven flow, as shown subsequently. The Kozeny–Carman relation for the permeability of packed beds of spheres and the drag coefficient for a single sphere (Stokes law) can be recovered from the interfacial drag correlation given in Table II upon making the appropriate simplifications for these limiting cases.

The number density of grains n is needed in the expression for the interfacial area concentration and, *via* the grain radius, in the calculation of the interfacial drag and species diffusion lengths (Table II). The grain density is taken to

Table I. Macroscopic Conservation Equations and Interfacial Balances ($k = s, l$, and $\varepsilon_s + \varepsilon_l = 1$)[26]

Mass: $\frac{\partial}{\partial t}(\varepsilon_k \rho_k) + \nabla \cdot (\varepsilon_k \rho_k \mathbf{v}_k) = \Gamma_k$

Interfacial mass balance: $\Gamma_s + \Gamma_l = 0$

Liquid momentum: $\frac{\partial}{\partial t}(\varepsilon_l \rho_l \mathbf{v}_l) + \nabla \cdot (\varepsilon_l \rho_l \mathbf{v}_l \mathbf{v}_l) = -\varepsilon_l \nabla p_l + \overline{\mathbf{v}}_s \Gamma_l + M_l^d + \varepsilon_l \rho_l g + \nabla \cdot \{\mu_l (\nabla(\varepsilon_l \mathbf{v}_l) + [\nabla(\varepsilon_l \mathbf{v}_l)]^t - \mathbf{v}_s \nabla \varepsilon_l - \nabla \varepsilon_l \mathbf{v}_s\}\}$

Solid velocity: $\mathbf{v}_s = V_c \mathbf{k}$

Interfacial liquid drag: $M_l^d = -\frac{3}{4}\frac{\varepsilon_s}{d_s} \rho_l C_{d\varepsilon} |\mathbf{v}_l - \mathbf{v}_s| (\mathbf{v}_l - \mathbf{v}_s)$

Mixture energy: $\frac{\partial}{\partial t}(\varepsilon_s \rho_s h_s + \varepsilon_l \rho_l h_l) + \nabla \cdot (\varepsilon_s \rho_s \mathbf{v}_s h_s + \varepsilon_l \rho_l \mathbf{v}_l h_l) = \nabla \cdot (\frac{k_s \varepsilon_s}{c_s} \nabla h_s + \frac{k_l \varepsilon_l}{c_l} \nabla h_l)$ where $h_s = c_{ps} T$ and $h_l = c_{pl} T + (c_{ps} - c_{pl}) T_e + \Delta h$

Species: $\frac{\partial}{\partial t}(\varepsilon_k \rho_k C_k) + \nabla \cdot (\varepsilon_k \rho_k \mathbf{v}_k C_k) = \nabla \cdot (D_k \rho_k \varepsilon_k \nabla C_k) + \overline{C}_{ki} \Gamma_k + \frac{S_v \rho_k D_k}{\ell_k^j} (\overline{C}_{ki} - C_k)$

Interfacial species balance: $(\overline{C}_{li} - \overline{C}_{si}) \Gamma_s = [\frac{S_v \rho_l D_l}{\ell_l} (\overline{C}_{li} - C_l) + \frac{S_v \rho_s D_s}{\ell_s} (\overline{C}_{si} - C_s)]$

Table II. Interfacial and Property Relations[26]

Interfacial area concentration: $S_v = (36\ \pi\ n)^{1/3}\ \varepsilon_s^{2/3}\ \delta(\varepsilon_s)$

where $\delta(\varepsilon_s) = 1$ for $\varepsilon_s \le \varepsilon_{sp}$; $\delta(\varepsilon_s) = \left(\frac{\varepsilon_s}{\varepsilon_{sp}}\right)^{1/3} \left(\frac{1 - \varepsilon_s}{1 - \varepsilon_{sp}}\right)^{\frac{1 - \varepsilon_{sp}}{\varepsilon_{sp}}}$ for $\varepsilon_s > \varepsilon_{sp}$

Radius of the solid grains: $R_s = d_s/2 = [\frac{3\varepsilon_s}{4\pi n}]^{1/3}$

Drag coefficient:[27]

$C_{d\varepsilon} = \{\frac{24 \times 2 C_{k\varepsilon} (1 - \varepsilon_l)}{\mathrm{Re}} + C_{i\varepsilon}\}$; $\mathrm{Re} = \frac{\varepsilon_l |\mathbf{v}_l - \mathbf{v}_s| d_s}{\nu_l}$

$C_{k\varepsilon} = 25/6$; $C_{i\varepsilon} = 7/3$ $\varepsilon_l \le 0.5$

$C_{k\varepsilon} = \frac{1}{2}\frac{\varepsilon_l^3}{1 - \varepsilon_l}[\frac{1 + 4.7 (1 - \varepsilon_l)}{1 - 1.83 (1 - \varepsilon_l)}]$; $C_{i\varepsilon} = \frac{24 (10^E - 1)}{\mathrm{Re}[1 - 0.9(\varepsilon_l - 0.25)^{1/3}(1 - \varepsilon_l)^{2/3}]^3}$ $\varepsilon_l > 0.5$

$\mathrm{E} = 0.261\mathrm{Re}^{0.369} - 0.105\mathrm{Re}^{0.431} - \frac{0.124}{1 + (\log_{10} \mathrm{Re})^2}$

Diffusion lengths:[28]

$\ell_l = [\frac{1}{\frac{1}{1 - \varepsilon_s^{1/3}} + \frac{1}{3\varepsilon_l} \mathrm{Sc}^{1/3}\mathrm{Re}^a}] R_s$; $a = \frac{2\mathrm{Re}^{0.28} + 4.65}{3(\mathrm{Re}^{0.28} + 4.65)}$

$\ell_s = \frac{R_s}{5}$

Liquid density relation:[29]

$$1/\rho_l = [0.397 - 4.5322 \times 10^{-3} C_l + 4.0924 \times 10^{-5} (T - 273.15) + 1.1078 \times 10^{-6} C_l (T - 273.15) + 2.7475 \times 10^{-5} C_l^2] \times 10^{-3}$$

Equilibrium phase diagram relations:

Primary solidification: $\overline{C}_{li} = \frac{C_e (T_m - T)}{T_m - T_e}$; $\overline{C}_{si} = \kappa \overline{C}_{li}$

Eutectic solidification: $T = T_e$; $\overline{C}_{li} = C_e$; $\overline{C}_{si} = C_e$

be uniform and equal to average values, as determined from the experiments of Finn *et al.*[10] A variable grain density was found to have a relatively small effect on the predicted macrosegregation.[32]

Table III. Thermophysical Properties and System Data[10,13,29,33]

Properties (Unit)	Numerical Value
Properties	
Density of primary solid phase, ρ_{sp} (kg/m^3)	2580.0
Density of eutectic solid phase, ρ_{se} (kg/m^3)	3409.0
Dynamic viscosity of the liquid phase μ_l (N s/m^2)	0.0012
Maximum solid packing fraction, ε_{sp}	0.637
Thermal conductivity of the liquid phase, k_l (W/m K)	57.3
Thermal conductivity of the solid phase, k_s (W/m K)	120.7
Specific heat of the liquid phase, c_{pl} (J/kg K)	1179.0
Specific heat of the solid phase, c_{ps} (J/kg K)	1032.0
Latent heat of phase change, Δh (J/kg)	392×10^3
Mass diffusivity of the liquid phase, D_l (m^2/s)	5.0×10^{-9}
Mass diffusivity of the solid phase, D_s (m^2/s)	8.0×10^{-13}
Segregation coefficient, κ	0.173
Eutectic temperature, T_e (K)	821.2
Eutectic species concentration, C_e (wt pct Cu)	32.7
Melting temperature of ''solvent,'' T_m (K)	933.5
System data	
Ingot diameter (m)	53.34×10^{-2}
Diameter of inlet (m)	0.127
Casting speed (m/s)	6.33×10^{-4}
Pour temperature T_0 (K)	980
Composition of pour, C_0 (wt pct Cu)	4.5
Inlet temperature of cooling water (K)	298
Cooling water flow rate per unit ingot circumference (m^2/h)	0.116

Table II also provides the relation adopted for the liquid density as a function of temperature and concentration.[29] Using this density relation in the buoyancy term in the momentum equation (Table I) implies that both thermal and solutal natural convection are taken into account. In the continuity equations, a fully variable liquid density, together with the primary and eutectic solid densities listed in Table III, allows for the calculation of contraction-driven flow before and during solidification. The contraction behavior of the present Al-4.5 wt pct Cu alloy during solidification is illustrated in Figure 1(a). For simplicity, the Scheil equation is used to relate the liquid temperature/concentration to the solid fraction. It can be seen that, before the eutectic reaction, there is a range of solid fractions where the volume increases during solidification. Due to this expansion, the total contraction during primary solidification is only slightly positive. Therefore, much of the contraction-driven flow is caused by the drastic density change during the eutectic reaction.

Partial remelting can possibly occur during continuous casting because of contraction of the ingot away from the mold, causing a rapid decrease in the heat transfer coefficient and reheating of the ingot shell. In the present study, it is assumed that, during remelting, the interfacial solid concentration is equal to the equilibrium value determined from the phase diagram. This approximation cannot be expected to be realistic but was confirmed[32] to have a negligible effect on the predictions presented here.

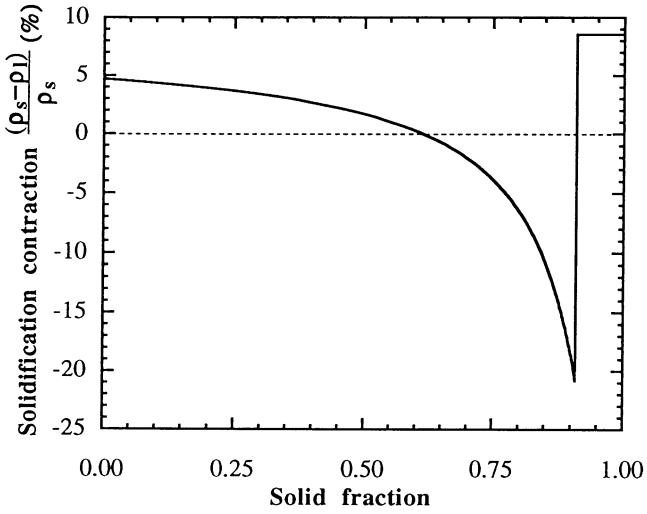

(*a*)

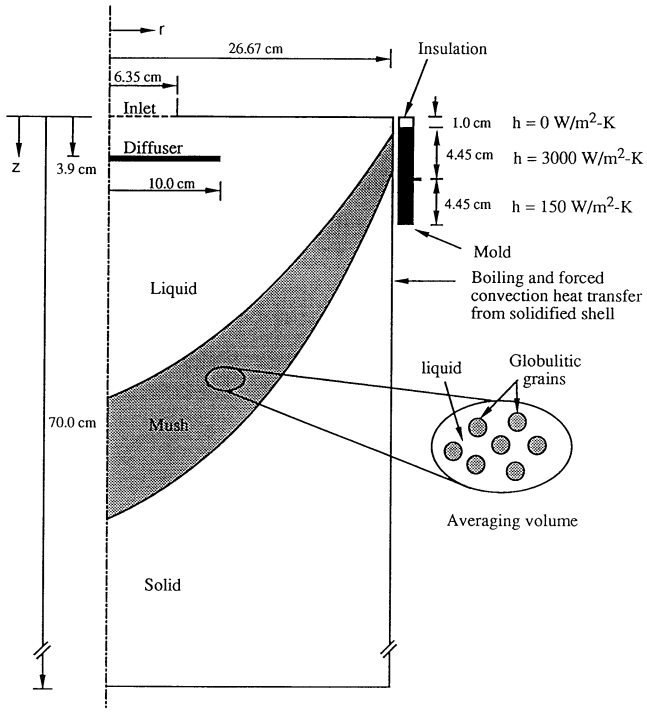

(*b*)

Fig. 1—Model illustration: (*a*) contraction behavior of the Al-4.5 wt pct Cu alloy during solidification; and (*b*) Schematic illustration of the domain and boundary conditions.

III. SYSTEM AND BOUNDARY CONDITIONS

A schematic of the DC continuous caster, very similar to the one employed by Finn *et al.*[10] and simulated in the present study, is shown in Figure 1(b) together with the relevant dimensions. The caster employed in the simulations differs from the one used by Finn *et al.* in that it has an extra ring of insulation (1-cm thick) above the mold. This insulation was added to ensure that a solid shell does not form all the way up to the top surface of the ingot, causing metal feeding problems and divergence of the numerical solution. The ingot is round with a diameter of 53.34 cm, and axial symmetry is assumed. The melt enters the mold with a composition of Al-4.5 wt pct Cu and a

Table IV. List of Simulations

Case	Grain Density n (m^{-3})	Additional Feature
Case 1	1.8×10^{11}	—
Case 2	5.0×10^{12}	—
Case 3	5.0×10^{12}	constant and equal densities, except buoyancy

temperature of 980 K (62 K superheat). A floating diffuser (steel), as indicated in Figure 1(b), is employed to redirect the incoming superheated melt toward the mold.

The heat transfer between the mold and the ingot is modeled by using a variable heat transfer coefficient. The top half of the mold is characterized by a heat transfer coefficient of 3000 W/m^2 K, whereas the one in the lower half drops to 150 W/m^2 K due to the contraction gap forming between the mold and the ingot shell. These values represent approximations of previous mold heat transfer measurements.[33] More sophisticated treatments of the mold boundary conditions are possible[20,34] and should be employed in future studies. Below the mold, water flows directly over the ingot surface and provides cooling by nucleate boiling and forced convection. This cooling is modeled using the heat transfer coefficient correlation developed by Weckman and Niessen.[35] The water enters the mold at a temperature of 298 K and a flow rate of 0.116 m^3/h/m of ingot circumference. An energy balance is used to calculate the axial variation of the bulk temperature of the cooling water. Inside the mold, a no-slip condition is used for the liquid velocity.

The solid ingot is withdrawn at the bottom at a casting speed of 3.81 cm/min. Thus, the melt velocity at the inlet (assumed uniform) can be calculated by global mass conservation. The length of the system is chosen such that in steady-state, axial conduction through the ingot at the lower boundary can be neglected. For simplicity, the top boundary next to the inlet is assumed to be adiabatic.

All system data and thermophysical properties used in the simulations are summarized in Table III. As a first approximation, all properties for each phase (except the liquid density) are assumed constant and independent of temperature and concentration.

IV. NUMERICAL PROCEDURES

The present model was implemented in the PHOENICS code (CHAM, N.A., Atlanta, GA) using a fixed-grid, single-domain, fully implicit solution procedure. Several modifications of the method described in Ni and Beckermann[26] were necessary due to (1) the use of a cylindrical coordinate system, (2) the use of a mixture energy equation instead of separate energy balances for each phase (this results in a considerable reduction in the computing time), (3) the setting of the solid velocity equal to the casting speed, (4) the accounting for contraction-driven flow due to the density changes, and (5) the presence of inflow and outflow boundary conditions. These and other procedures are detailed in the thesis by Reddy.[32]

The computational grid employed in the present study consisted of 60×80 control volumes in the radial and axial directions, respectively. The grid was heavily biased near the mold in an effort to better resolve the large solid fraction, velocity, temperature, and species concentration gradients in this region. A relatively coarse grid was used in the lower portion of the domain where a fully solid region is expected to be present and heat diffusion is the only mode of transport.

Only the steady-state solution is of interest in this study and was approached using time steps of 0.5 seconds. The simulations took about 1500 seconds on the average to reach steady state. One second of simulation took about 1 minute of time on an IBM*-3090 computer.

*IBM is a trademark of International Business Machines Corp., Armonk, NY.

V. RESULTS, DISCUSSION, AND COMPARISON WITH EXPERIMENT

The results of three simulations are presented here, as summarized in Table IV. Case 1 is compared to the grain-refined experiment of Finn *et al.*[10] and uses a grain density of 1.8×10^{11} m^{-3}. This average grain density was measured directly from the micrographs presented as Figure 6 in Finn *et al.* The intercept method was employed to calculate the grain density using an empirical relation.[36] Grain density is inversely related to grain size, which, in turn, affects primarily the permeability of and flow through the mush. The second simulation assumes a higher grain density of 5×10^{12} m^{-3}. This value represents an average obtained from the cell sizes plotted in Figure 7 (for the same experiment) in Finn *et al.* The reason for the discrepancy between the values from Figures 6 and 7 in Finn *et al.* is not known, but it is likely that the values reported in Figure 7 are incorrect (see subsequent discussion). If the grain density in case 2 is converted into a spacing, this spacing is actually very close to the average secondary dendrite arm spacing in the non-grain-refined experiment of Finn *et al.* The higher grain density in case 2 translates into a less permeable mushy zone and, thus, a different macrosegregation pattern can be expected. To study the effect of contraction-driven flow on macrosegregation, case 3 neglects contraction-driven flow, *i.e.*, the solid densities are set equal to the nominal liquid density. Liquid density changes are considered only in the buoyancy term in the momentum equation.

A. *Case 1*

Figure 2 shows a plot of the predicted isotherms for case 1 ($n = 1.8 \times 10^{11}$ m^{-3}). This figure shows the entire computational domain (in scale). It can be seen that the isotherms at the lower boundary are relatively vertical, justifying the choice of the domain length. Also, there exist strong temperature gradients next to the mold and next to the water-cooled surface. The liquidus (918 K) and eutectic (821 K) isotherms approximately demarcate the mushy zone, with single-phase liquid above the liquidus and fully solid below the eutectic. The temperature gradients are relatively small in the fully liquid region because of convective mixing.

The liquid velocity field and solid fraction contours in the upper part of the domain are shown in Figure 3 (in scale). In the pure solid region, for plotting purposes, the

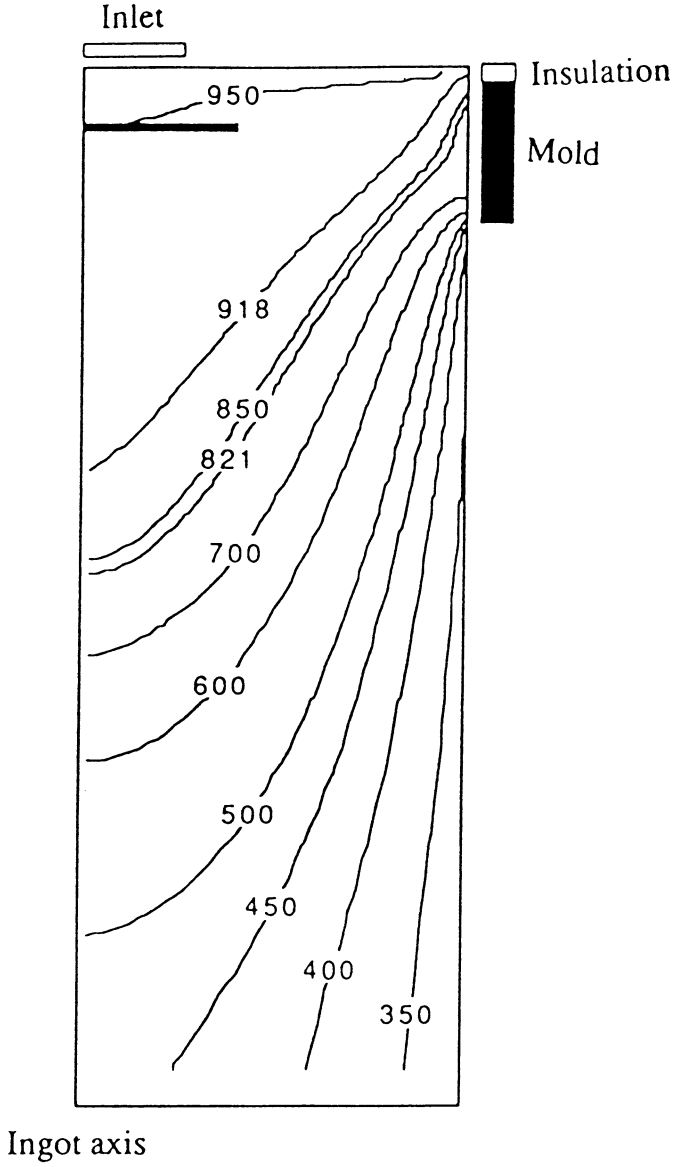

Fig. 2—Predicted isotherms in case 1.

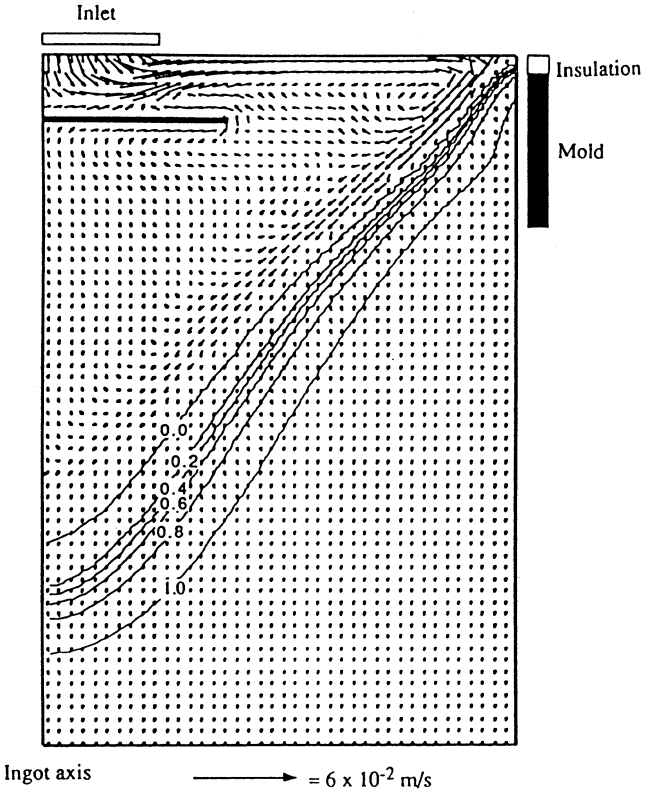

Fig. 3—Predicted liquid velocity field and solid fraction contours in case 1.

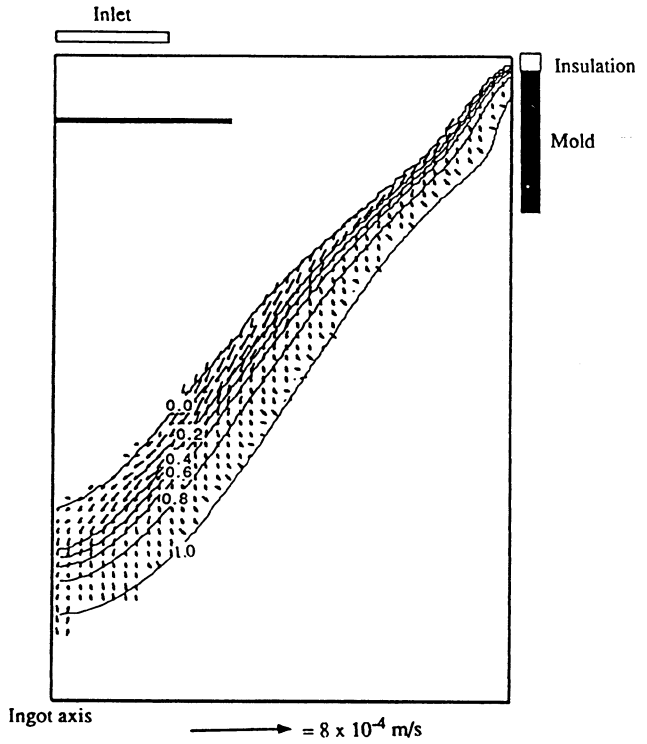

Fig. 4—Predicted relative velocity field, ($\mathbf{v}_l - \mathbf{v}_s$), and solid fraction contours in case 1.

liquid velocity is set equal to the solid velocity, which, in turn, is equal to the casting speed. The liquid melt enters the mold through the inlet opening at the top and then is redirected by the diffuser and flows along the upper liquid surface toward the mold. Due to primarily thermal buoyancy forces, the melt then flows down along the interface between the mush and the pure liquid region toward the centerline. The mushy zone almost reaches the top surface of the mold and a fully solid shell is present over the lower part of the mold.

Figure 4 shows a plot of the relative velocity field, ($\mathbf{v}_l - \mathbf{v}_s$), with the solid fraction contours superimposed. Note that the velocity scale is about two orders of magnitude smaller than in Figure 3, allowing for a better visualization of the flow in the mush. The velocities are smaller in the mush because of the interfacial drag. Nonetheless, this flow is responsible for the macrosegregation. Liquid density increases as solidification proceeds and solutal buoyancy augments thermal buoyancy. The buoyancy forces result in a relatively strong flow along the mushy zone toward the ingot axis in the region of lower solid fraction ($\varepsilon_s < 0.6$). In the regions of higher solid fraction, the mush is less permeable, and the relative velocities are somewhat smaller.

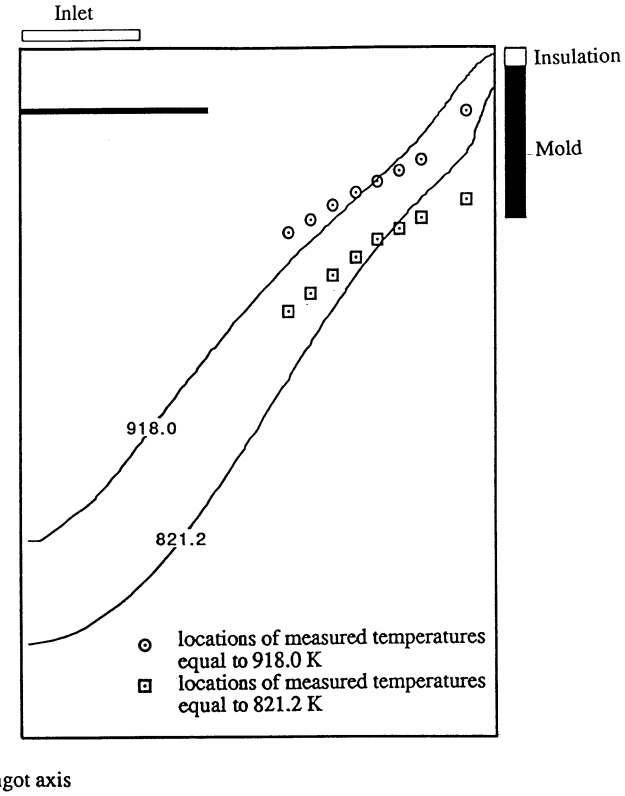

Fig. 5—Comparison of predicted liquidus and eutectic isotherms in case 1 (lines) with temperature measurements of Finn *et al.*[10] (symbols).

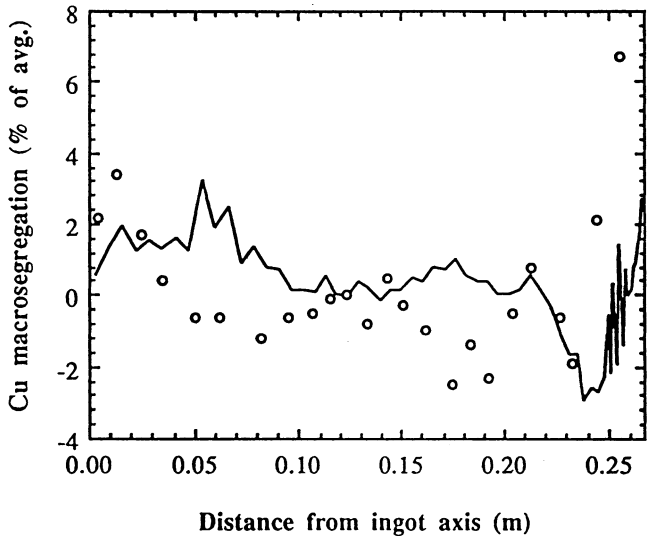

Fig. 6—Comparison of predicted radial macrosegregation profile in case 1 (line) with data from the grain-refined experiment of Finn *et al.*[10] (symbols).

Here, the flow is primarily due to solidification contraction upon eutectic formation. This flow is toward the eutectic front, *i.e.*, the solid fraction contour corresponding to unity.

Figure 5 shows a comparison of temperatures measured in the grain-refined experiment of Finn *et al.*[10] with the prediction of case 1. Only the 821.2 K and 918.0 K isotherms are plotted. The former is equal to the eutectic temperature, whereas the latter corresponds to the liquidus temperature evaluated at the nominal composition C_0. The

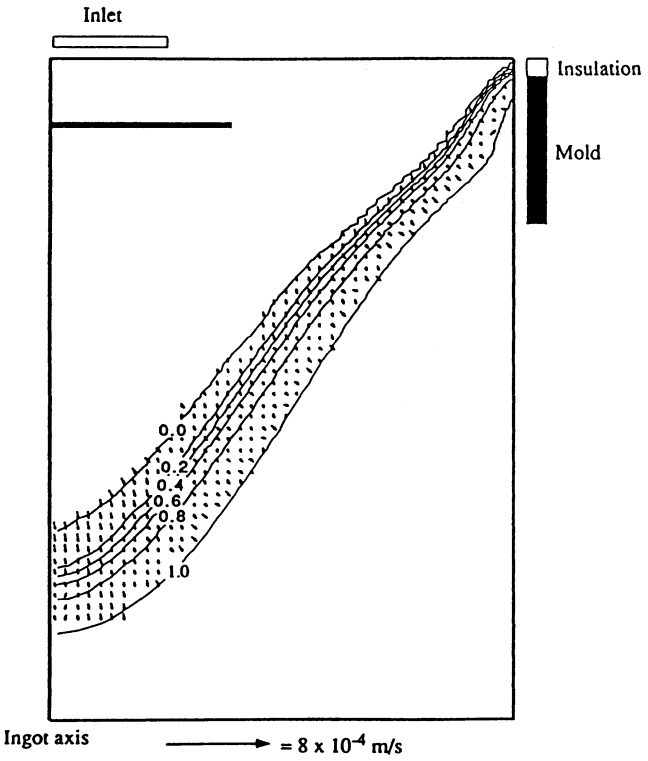

Fig. 7—Predicted relative velocity field, ($\mathbf{v}_l - \mathbf{v}_s$), and solid fraction contours in case 2.

locations of the measured temperatures were extracted from Figure 4 in Finn *et al.* Considering the difficulty of exactly locating the thermocouples in the experiments, the agreement between the measurements and predictions is reasonable. Near the mold the predicted temperatures lie above the measured ones. The difference can be primarily attributed to uncertainties in the modeling of the mold heat transfer (the insulated region did not exist in the experiments and the contraction gap probably formed lower in the mold than assumed). Closer to the ingot axis, the predicted isotherms lie below the experimental data points. This disagreement is most likely due to the assumption of a constant thermal conductivity of the solid metal (in reality, the conductivity varies by almost a factor of 2 between room and melting temperatures) and uncertainties in the correlation used for the ingot surface heat transfer coefficient.[35] No temperature measurements are available near the ingot axis due to the presence of the diffuser below the inlet. Although better agreement between the measured and predicted temperatures could readily be obtained by iterating on the thermal boundary conditions and using variable thermophysical properties, the predicted sump shape was deemed to be sufficiently realistic to allow for the present investigation of macrosegregation.

The predicted radial variation of macrosegregation is plotted in Figure 6 and compared to experimental data from the grain-refined experiment.[10] The measured and predicted segregation is positive at both the surface and the centerline of the ingot. The advection of solute-rich liquid through the mush both toward the ingot shell (by contraction flow) and the centerline (by thermosolutal convection) results in a solute-poor region at about 3 cm from the ingot outer surface. A comparison of the predictions with the

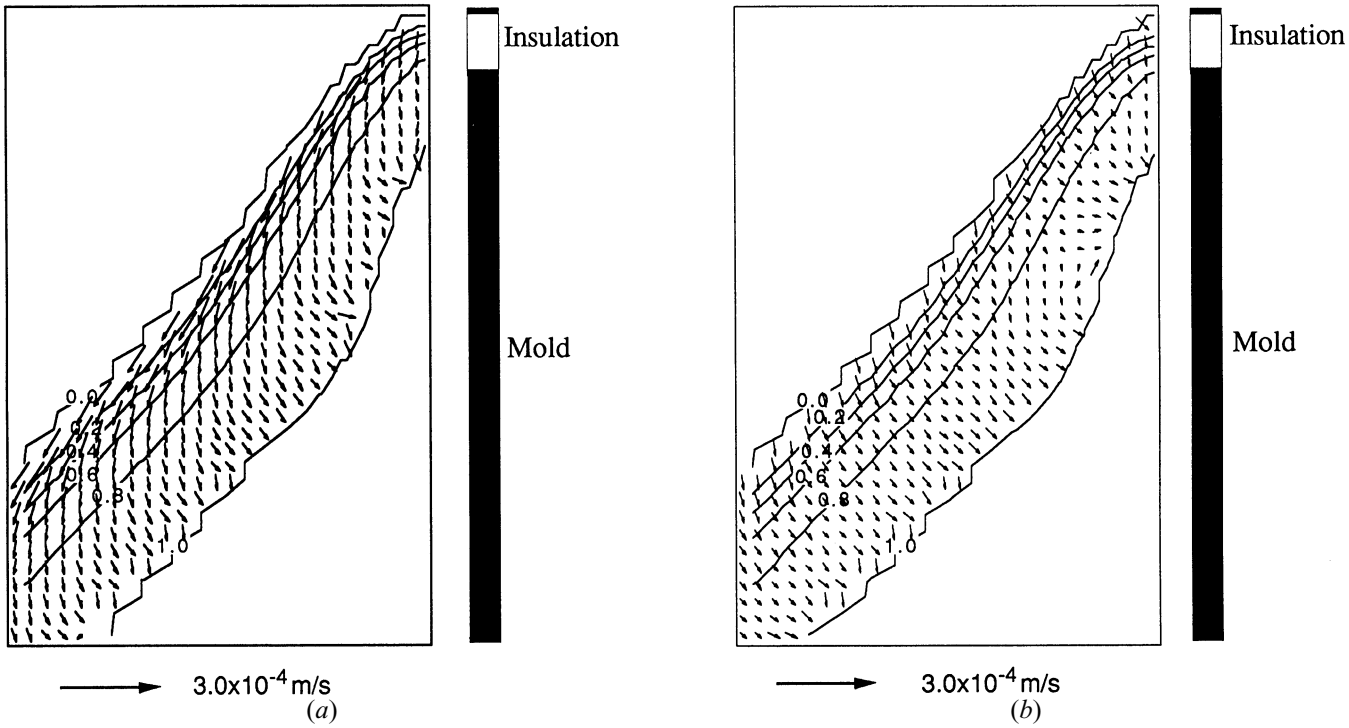

Fig. 8—Enlargement of the predicted relative velocity field, ($\mathbf{v}_l - \mathbf{v}_s$), and solid fraction contours adjacent to the mold in (*a*) case 1 and (*b*) case 2.

measurements shows that, at the outer surface, the experimental value of the segregation is significantly higher than the prediction. In the experiment, it was found that the solidified shell had contracted away from the mold wall, making the ingot diameter smaller than the nominal diameter used in the simulations. This shift in the location of the outer surface makes a direct comparison of the measured and predicted macrosegregation patterns near the outer surface difficult. Exudation, porosity formation,[37] measurement difficulties, and inaccuracies in the modeling of the mold heat transfer (discussed earlier) may all be contributors to the disagreement for the outermost datum. Away from the surface, the segregation pattern appears to be reasonably well predicted. Both the simulation and the measurements show similar degrees of positive centerline segregation (about +2 pct, if smoothed), indicating that the thermosolutal convection through the mush toward the centerline was well predicted. This is, of course, only possible if a reasonably accurate value of the grain density is used in the expression for the drag coefficient (Table II). Apparently, the direct measurement from the micrograph of Figure 6 in Finn *et al.*[10] produced such a value. Note that both the measured and predicted macrosegregation data show a large amount of scatter, which would be difficult to match exactly. The reason for the scatter is presently not known. In fact, replicate measurements by Finn *et al.* show deviations that are similar in magnitude as those in Figure 6 (except at the outer surface).

Finally, the predicted eutectic volume fraction in case 1 (not plotted) is, on the average, equal to 6.3 pct. Variations over the ingot cross section result from changing cooling rates and macrosegregation, but all fractions are within about 5 pct of the average value. For comparison, the eutectic fraction calculated from the Scheil equation is about 9.1 pct for an Al-4.5 wt pct Cu alloy. The lower mean value predicted in case 1 is primarily due to the inclusion of backdiffusion in the model and agrees well with the measured and predicted eutectic fractions (for a similar cooling rate and composition) plotted in Figure 6 of Reference 24. The eutectic fraction was not measured by Finn *et al.*,[10] making a more direct comparison impossible.

B. *Case 2*

The grain density in case 2 ($n = 5 \times 10^{12}$ m^{-3}) is more than an order of magnitude higher than in case 1. Consequently, the mushy zone is less permeable, and thermosolutal convection in the mush can be expected to be weaker. In the present simulations, porosity formation is neglected. In reality, porosity could result if the mushy zone is sufficiently impermeable so as to cut off metal feeding to the regions undergoing contraction.[37]

The temperature and liquid velocity fields are quite similar to those in case 1 and, hence, are not reproduced from Reference 32. Much different is the predicted relative velocity field presented in Figure 7. The same velocity scale as in Figure 4 (case 1) is used. For better visualization and direct comparison, Figure 8 shows an enlargement of the relative velocity field and solid fraction contours in cases 1 and 2 in the region adjacent to the mold. Although some of the velocity vectors and kinks in the solid fraction contours appear unrealistic, which is simply caused by the large interpolations required for this magnification, the plots clearly illustrate the differences in the flow patterns between the two cases. The effect of a less permeable mushy zone in case 2 is seen in the smaller relative velocities, especially at low solid fractions. Because of the lower permeability, thermosolutal buoyancy forces are not effective enough to produce a significant flow toward the ingot axis. In case 2, the flow in the mushy zone is predominantly

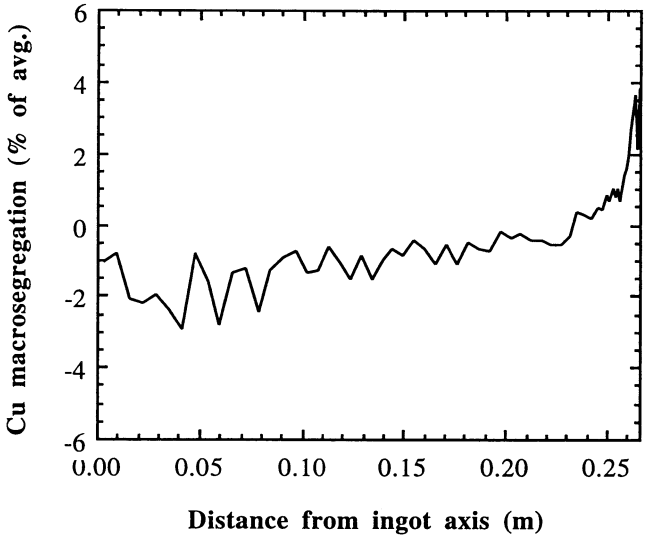

Fig. 9—Predicted radial macrosegregation profile in case 2.

driven by solidification contraction upon eutectic formation, causing the liquid to flow almost exclusively toward the eutectic front. Only near the eutectic front are the velocities similar in both cases. Also note, from Figure 8, that the flow next to the mold is far from being unidirectional (*i.e.*, only toward the outer surface) because of the inclination and curvature of the solid fraction contours.

The predicted radial variation of macrosegregation in the fully solid region is plotted in Figure 9. The inverse segregation near the ingot surface is similar in extent to that in case 1. However, there is no minimum in the profile away from the surface, the concentration decreases continuously toward the centerline, and the centerline segregation is negative. As mentioned previously, the flow in the mushy zone in case 2 is dominated by contraction and, hence, the liquid flows toward the $\varepsilon_s = 1.0$ contour. This flow has a radial velocity component toward the outer ingot surface, and, consequently, solute-rich liquid is advected away from the ingot axis resulting in the negatively segregated central region. A comparison of the macrosegregation patterns predicted in cases 1 and 2 (Figures 6 and 9, respectively) provides a direct measure of the importance of thermosolutal convection in the mush, because such convection is virtually absent in case 2 (while the contraction flow is about the same).

Clearly, the permeability of the mush in case 2 is too low, and hence the grain density too high, to predict the positive centerline segregation measured in the grain-refined experiment of Finn *et al.*[10] However, another experiment by Finn *et al.*, featuring a non-grain-refined and dense columnar dendritic microstructure does confirm that a less permeable mush results in negative centerline segregation. In fact, the centerline segregation of about −2 pct measured in this experiment[10] compares very well with the predicted centerline value in case 2 (Figure 9), indicating that, in both the non-grain-refined experiment and the simulation of case 2, thermosolutal convection in the mush is negligibly small. Furthermore, this comparison establishes considerable confidence in the present prediction of the extent of the contraction-driven flow and its effect on macrosegregation. As already noted, the spacing of the grains in case 2, as can be calculated from the grain density, is about equal to the secondary dendrite-arm spacing measured in the non-grain-refined experiment of Finn *et al.*, which indicates that the interfacial drag (or permeability) expression in the model can be used for both grain-refined globulitic and non-grain-refined dendritic microstructures if the characteristic length in the expression is chosen properly.

The average value of the predicted eutectic volume fraction is equal to about 5.3 pct in case 2. This fraction is, as expected, lower than in case 1 (6.3 pct), because the microstructure in case 2 is much finer, resulting in a higher back-diffusion rate.[31] As for permeability, the grain density (or spacing) used in the back-diffusion expression should be translated into a secondary dendrite-arm spacing for the highly dendritic structure in the non-grain-refined experiment simulated in case 2.

C. *Case 3*

This simulation was carried out to study the effects of neglecting contraction-driven flow on the macrosegregation pattern. Thermosolutal convection is included and the same grain density is used as in case 2.

Not surprisingly, the thermal field and the liquid velocities in the sump are very similar to cases 1 and 2.[32] The macrosegregation profile, Figure 10, shows that, as expected, positive surface (*i.e.*, inverse) segregation is absent in case 3 because of the neglect of contraction-driven flow. In fact, macrosegregation vanished almost completely, with the remaining nonuniformities in concentration being caused by the very weak thermosolutal convection through the relatively impermeable mush (because the same high grain density as in case 2 was utilized). Thus, a comparison of cases 2 and 3 (Figures 9 and 10, respectively) gives a direct measure of the importance of accounting for contraction-driven flow in predicting macrosegregation in the present system. Most importantly, the contraction flow not only causes inverse segregation near the ingot surface, but also has a considerable effect on the macrosegregation pattern in the central portion of the ingot.

VI. CONCLUSIONS

A modified version of the two-phase model of Ni and Beckermann was used to simulate the DC continuous casting of an Al-Cu round ingot. The model assumes a rigid and attached solid and features thermosolutal buoyancy and contraction-driven melt convection, heat transfer, and solute redistribution on the system scale, and grain growth, microsegregation, and solutal undercooling of the liquid on a microscopic scale. Results of three different simulations are presented. Comparisons with the results of experiments by Finn *et al.*[10] are also attempted. Better agreement with the measured temperatures could be obtained by making some adjustments in the thermal boundary conditions and using more accurate thermophysical properties. Nonetheless, the results show that the model is able to predict important macrosegregational features.

The effect of grain density on the flow in the mush and centerline macrosegregation is studied in two simulations. Centerline segregation is a result of two opposing flows in the mushy zone: (1) contraction-driven flow transports sol-

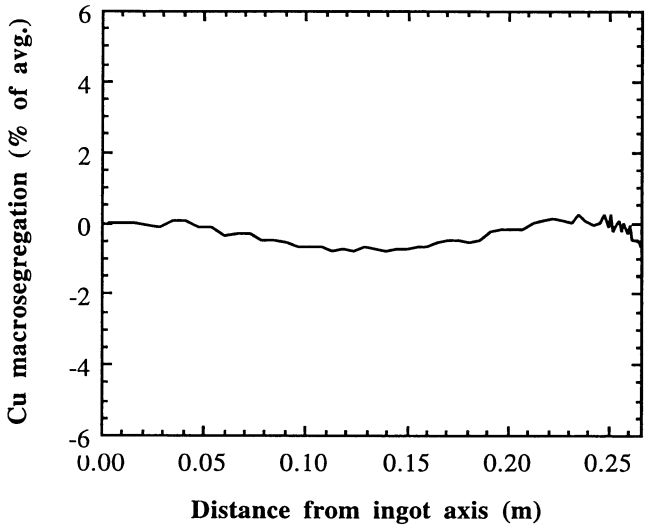

Fig. 10—Predicted radial macrosegregation profile in case 3.

ute-rich liquid away from the ingot center toward the outer surface and, hence, tends to negatively segregate the central region of the ingot; and (2) thermosolutal buoyancy-induced flow, on the other hand, transports solute-rich liquid toward the ingot center, thus tending to cause positive centerline segregation. The sign (positive or negative) and extent of the centerline segregation, therefore, are determined by which of these two flows dominate in the mushy zone, which in turn depends directly on the permeability of the mush as dictated by the grain density. Although the preceding finding may not be new, the present model calculates these flows from the basic conservation equations and is able to predict the resulting macrosegregation pattern using actual, measured grain densities (for grain-refined ingots) or secondary dendrite-arm spacings (for non-grain-refined ingots). The next step in modeling would, thus, be the inclusion of reliable relations for the prediction of the microstructure as a function of the solidification conditions and grain-refinement practice.

A comparison of two simulations with and without contraction-driven flow demonstrates how this flow not only causes inverse segregation near the outer surface, but also influences centerline segregation. Further research is required to more accurately predict the exact magnitude of the macrosegregation at the ingot surface, something that will require the inclusion of exudation in the model.

One potential shortcoming of the present simulations is that the transport of free grains is neglected. The duplex grain structure found at the centerline in the grain-refined experiment of Finn *et al.*[10] can be considered evidence of such transport.[2] However, the present predictions, neglecting grain transport, appear to provide approximately correct levels of centerline segregation when compared to both the grain-refined and non-grain-refined experiments of Finn *et al.* Clearly, more simulations and experiments are needed to clarify this issue.

NOMENCLATURE

a	coefficient in Table II	C	concentration of Cu (wt pct)
c_p	specific heat (J/kg K)	$C_{d\varepsilon}$	generalized drag coefficient
d_s	grain diameter (m)	D	diffusion coefficient (m^2/s)
E	coefficient in Table II	g	gravitational acceleration (m/s^2)
h	enthalpy (J/kg) or convective heat-transfer coefficient (W/m^2 K)	k	thermal conductivity (W/m K)
$\mathbf{k}$	unit vector in axial direction	l	diffusion length (m)
M_l^d	interfacial drag (N/m^3)	n	grain density ($1/m^3$)
p	pressure (N/m^2)	r	radial coordinate (m)
R_s	grain radius (m)	Re	multiphase Reynolds number
Sc	Schmidt number	S_v	interfacial area concentration (1/m)
t	time (s)	T	temperature (K)
$\mathbf{v}$	velocity vector (m/s)	V_c	casting speed (m/s)
z	axial coordinate (m)		

Greek Symbols

δ	impingement function	κ	partition coefficient
Δh	latent heat of fusion (J/kg)	μ	dynamic viscosity (kg/s m)
ε	volume fraction	ν	kinematic viscosity (m^2/s)
Γ	interfacial mass-transfer rate due to phase change (kg/m^3 s)	ρ	density (kg/m^3)

Subscripts

e	eutectic	m	pure solvent
i	interfacial	o	initial or inlet
k	phase	p	packing or primary
l	liquid	s	solid

Superscripts

—	interfacial average	t	transpose

ACKNOWLEDGMENTS

This work was supported by the National Science Foundation under Grant No. CTS-8957149 and by the Alcoa Technical Center (Alcoa Center, PA). Discussions with Drs. D.P. Ziegler and W.D. Bennon, both of the Alcoa Technical Center, are gratefully acknowledged.

REFERENCES

1. M.G. Chu and J.E. Jacoby: *Light Met.*, 1990, pp. 925-30.
2. H. Yu and D.A. Granger: *Aluminum Alloys: Their Physical and Mechanical Properties*, Proc. Int. Conf., Charlottesville, VA, EMAS, United Kingdom, 1986, vol. 1, pp. 17-29.
3. H. Kastner: *Z. Metallk.*, 1950, vol. 41, pp. 193-205 and 247-54.
4. K. Buxmann: *Metallurgy*, 1977, vol. 31, pp. 163-70.
5. R. Ellerbrok and S. Engler: *Metallurgy*, 1983, vol. 37, pp. 784-88.
6. L. Ohm and S. Engler: *Metallurgy*, 1989, vol. 43, pp. 520-24.
7. M.C. Flemings and G.E. Nereo: *Trans. TMS-AIME*, 1967, vol. 239, pp. 1449-61.
8. M.C. Flemings, R. Mehrabian, and G.E. Nereo: *Trans. TMS-AIME*, 1968, vol. 242, pp. 41-49.
9. R. Mehrabian, M. Keane, and M.C. Flemings: *Metall. Trans.*, 1970, vol. 1, pp. 1210-20.
10. T.L. Finn, M.G. Chu, and W.D. Bennon: in *Micro/Macro Scale Phenomena in Solidification*, C. Beckermann, L.A. Bertram, S.J. Pien, and R.E. Smelser, eds., ASME, New York, NY, 1992, HTD-vol. 218/AMD-vol. 139, pp. 17-26.
11. B. Gariepy and Y. Caron: *Light Met.*, 1991, pp. 961-71.

12. S.C. Flood, L. Katgerman, A.H. Langille, S. Rogers, and C.M. Read: *Light Met.*, 1988, pp. 943-47.
13. S.C. Flood, L. Katgerman, and V.R. Voller: in *Modeling of Casting, Welding and Advanced Solidification Processes V*, M. Rappaz, M.R. Ozgu, and K.W. Mahin, eds., TMS, Warrendale, PA, 1991, pp. 683-90.
14. B.Q. Li, J.C. Liu, and J.A. Brock: in *EDP Congr.*, TMS, Warrendale, PA, 1992, pp. 841-57.
15. B.Q. Li and P.N. Anyalebechi: in *Transport Phenomena in Solidification*, C. Beckermann, H.P. Wang, L.A. Bertram, M.S. Sohal, and S.I. Guceri, eds., ASME, New York, NY, 1994, HTD-vol. 284, AMD-vol. 182, pp. 97-107.
16. Ch. Raffourt, Y. Fautrelle, J.L. Meyer, and B. Hannart: in *Modeling of Casting, Welding and Advanced Solidification Processes V*, M. Rappaz, M.R. Ozgu, and K.W. Mahin, eds., TMS, Warrendale, PA, 1991, pp. 691-98.
17. C. Devadas and J.F. Grandfield: *Light Met.*, 1991, pp. 883-92.
18. G.U. Grün, I. Eick, and D. Vogelsang: *Light Met.*, 1994, pp. 863-69.
19. A.V. Reddy and C. Beckermann: in *Materials Processing in the Computer Age II*, V.R. Voller, S.P. Marsh, and N. El-Kaddah, eds., TMS, Warrendale, PA, 1994, pp. 89-102.
20. A. Hakonsen and D. Mortensen: in *Modeling of Casting, Welding and Advanced Solidification Processes VII*, M. Cross and J. Campbell, eds., TMS, Warrendale, PA, 1995, pp. 763-70.
21. J. Ni and C. Beckermann: *Metall. Trans. B*, 1991, vol. 22B, pp. 349-61.
22. C. Beckermann and C.Y. Wang: in *Annual Review of Heat Transfer VI*, C.L. Tien, ed., Begell House, New York, NY, 1995, pp. 115-98.
23. P.J. Prescott and F.P. Incropera: in *Advances in Heat Transfer*, D. Poulikakos, ed., Academic Press, New York, NY, 1996, vol. 28, pp. 231-338.
24. S.C. Flood, P.A. Davidson, and S. Rogers: in *Modeling of Casting, Welding and Advanced Solidification Processes VII*, M. Cross and J. Campbell, eds., TMS, Warrendale, PA, 1995, pp. 801-08.
25. E. Haug, A. Mo, and H.J. Thevik: *Int. J. Heat Mass Transfer*, 1995, vol. 38, pp. 1553-63.
26. J. Ni and C. Beckermann: *J. Mater. Processing Manufacturing Sci.*, 1993, vol. 2, pp. 217-31.
27. P.K. Agarwal and B.K. O'Neill: *Chem. Eng. Sci.*, 1988, vol. 43 (9), pp. 2487-99.
28. P.N. Rowe and K.T. Claxton: *Trans. Inst. Chem. Eng.*, 1965, vol. 43, pp. T321-T331.
29. S. Ganesan and D.R. Poirier: *Metall. Trans. A*, 1987, vol. 18A, pp. 721-23.
30. C.Y. Wang and C. Beckermann: in *Materials Processing in the Computer Age II*, V.R. Voller, S.P. Marsh, and N. El-Kaddah, eds., TMS, Warrendale, PA, 1994, pp. 129-43.
31. C.Y. Wang and C. Beckermann: *Mater. Sci. Eng. A*, 1993, vol. A171, pp. 199-211.
32. A.V. Reddy: Ph.D. Thesis, University of Iowa, Iowa City, IA, 1995.
33. D.P. Ziegler: Alcoa Technical Center, Alcoa Center, PA, private communication, 1994.
34. M. Rappaz, J.L. Desbiolles, J.M. Drezet, Ch.A. Gandin, A. Jacot, and Ph. Thevoz: in *Modeling of Casting, Welding and Advanced Solidification Processes VII*, M. Cross and J. Campbell, eds., TMS, Warrendale, PA, 1995, pp. 449-57.
35. D.C. Weckman and P. Niessen: *Metall. Trans. B*, 1992, vol. 23B, pp. 593-602.
36. R.T. DeHoff and F.N. Rhines: *Quantitative Microscopy*, McGraw-Hill Book Company, New York, NY, 1968.
37. P. Rousset, M. Rappaz, and B. Hannart: *Metall. Trans. A*, 1995, vol. 26A, pp. 2349-58.